

Photocatalytic Methane Conversion to C1 Oxygenates over Palladium and Oxygen Vacancies Co-Decorated TiO₂

Zhuyu Gong, Lei Luo,* Chao Wang, and Junwang Tang*

Direct methane conversion to value-added chemicals through photocatalysis is promising but still has great challenges in both efficient activation of C–H bonds and suppression of over-oxidation. Herein, palladium nanoparticles and oxygen vacancies (OVs) co-modified TiO₂ photocatalysts are prepared and employed for photocatalytic CH₄ conversion at room temperature. Under optimized conditions with O₂ and water as the oxidants, a high yield of liquid oxygenates, e.g., 54 693 μmol g⁻¹ h⁻¹ with a nearly 100% selectivity has been achieved.

Mechanism investigations reveal that Pd and OVs synergistically promote charge separation, with Pd and OVs acting as hole and electron acceptors, respectively. Isotopic experiments elucidate that both H₂O and O₂ are oxygen sources for oxygenate production, where O₂ is the predominant one.

Photocatalysis has emerged as the green pathway to activate CH₄ under mild conditions through the injection of a photo-induced charge carrier instead of thermal energy.^[6] The key to efficient photocatalytic CH₄ conversion lies in the development of a suitable photocatalyst. Recently, ZnO loaded with noble metal was reported to convert CH₄ into liquid oxygenates, with oxygen (O₂) as the oxidant.^[7] Au₁-BP promoted CH₄ conversion into CH₃OH with the reactive hydroxyl radicals (OH), which are formed by O₂ with the assistance of water under light irradiation.^[8] It is clear that the predominant challenge lies in simultaneous regulation of both activation of CH₄ and selectivity of desired products.

Suitable co-catalysts like Au and Pd were reported to be the hole/electron acceptors to promote charge separation,^[9] as well as accelerating H₂O oxidation and O₂ reduction to generate reactive oxygen species. Such encouraging advances then provide to some extent understanding of both charge dynamics and surface kinetics during photocatalytic CH₄ activation. Besides co-catalysts modification, surface engineering is the other way to promote charge dynamics.^[10] It was reported that oxygen vacancies (OVs) and metastable Ti³⁺ played a vital role in determining the photocatalytic performance of TiO₂, especially due to the n-type doping and the improved carrier density.^[10c,11] Moreover, interfacial resistance could also be regulated through surface engineering.^[12] In parallel, surface kinetics could also be optimized by the introduction of surface defects by providing additional chemical adsorption and reactive sites.^[13] Given these aforementioned attractive potentials of co-catalyst and OVs modification, the synergy of both would largely promote charge separation and surface reactions.

Besides the design of suitable photocatalysts, reaction conditions including oxidant, solvent, pressure, and reaction time during CH₄ conversion are also important taking into account the reaction kinetics. Though it is difficult to gain an efficient activity due to the low solubility of CH₄ in H₂O, H₂O oxidation into ·OH radicals was reported to be essential in the activation of CH₄.^[14] Meanwhile, H₂O could also promote the desorption of the oxygenate products and avoid over-oxidation of CO₂.^[15] In parallel, a high pressure would increase the concentration of reactants, and a long reaction time might result in deep oxidation. Moreover, the oxidants are also important. Compared with H₂O₂, O₂ is much more benign and economically available, which is beneficial for future industrial application.^[16] Therefore, it is critical to study the influence of the reaction conditions on CH₄ conversion.


Herein, Pd nanoparticles and OVs co-modified TiO₂ photocatalyst were designed to drive CH₄ conversion with O₂ as the

1. Introduction

As the principal constituent of natural/shale gases, methane (CH₄) is a promising industrial feedstock for manufacturing value-added chemicals.^[1] However, efficient CH₄ conversion is still of a great challenge owing to its high C–H bond energy (439 kJ mol⁻¹), low electron affinity (−1.9 eV), and high ionization energy (12.6 eV).^[2] The current industrial CH₄ conversion via dry/steam-reforming^[3] and subsequent Fischer–Tropsch synthesis^[4] is an energy-intensive and indirect route, where high temperature (>700 °C) is required.^[5] Accordingly, direct CH₄ conversion under mild conditions is highly desired.

Z. Gong, L. Luo
Key Lab of Synthetic and Natural Functional Molecule Chemistry of
Ministry of Education
The Energy and Catalysis Hub
College of Chemistry and Materials Science
Northwest University
Xi'an 710127, P. R. China
E-mail: luol@nwu.edu.cn

C. Wang, J. Tang
Department of Chemical Engineering
University College London
London WC1E 7JE, UK
E-mail: Junwang.tang@ucl.ac.uk

 The ORCID identification number(s) for the author(s) of this article can be found under <https://doi.org/10.1002/solr.202200335>.

© 2022 The Authors. Solar RRL published by Wiley-VCH GmbH. This is an open access article under the terms of the Creative Commons Attribution License, which permits use, distribution and reproduction in any medium, provided the original work is properly cited.

DOI: 10.1002/solr.202200335

oxidant in an aqueous solution. The optimized production rate of C1 oxygenate products reached $54\,693\ \mu\text{mol g}^{-1}\text{h}^{-1}$ with $\approx 98.6\%$ selectivity. Mechanism investigations proved that Pd and OV_s acted as the hole and electron acceptors, respectively, making a synergetic contribution to inhibit charge recombination and activate both methane and oxygen gas. Furthermore, the reaction pathway and the oxygen source including O₂ and H₂O were discussed according to the isotopic experiments.

2. Results and Discussion

2.1. Structural Identification

X-ray diffraction (XRD) patterns were conducted to study the phase of crystals. As shown in Figure 1a, XRD patterns displayed the anatase TiO₂ structure (PDF#21-1272) of TiO₂, def-TiO₂, and Pd_{0.5}-def-TiO₂. The characteristic diffraction peaks remained the same for all samples. No Pd-associated diffraction peak was observed, indicating the low loading amount or uniform distribution of Pd species. Electron paramagnetic resonance (EPR) spectra were applied to study the unpaired electrons of the catalysts. In Figure 1b, both TiO₂ and def-TiO₂ exhibited a similar EPR signal at $g = 2.003$, which was attributed to OV_s.^[17] The

improved EPR intensity on def-TiO₂ indicated the successful introduction of OV_s into def-TiO₂ during calcination with urea. In addition, Pd_{0.5}-def-TiO₂ showed the largest intensity of OV_s, which implied that the Pd species loading might be beneficial to more OV_s formation by reducing the formation energy of OV_s.^[18] As shown in Figure S1, Supporting Information, the corresponding low-magnification transmission electron microscope (TEM) images of TiO₂ and def-TiO₂ exhibited that the pristine TiO₂ and def-TiO₂ photocatalysts were nanoparticles. The lattice fringe of $d = 0.36\ \text{nm}$ was indexed to the (101) facet of anatase TiO₂. Moreover, the high-resolution TEM (HRTEM) image of def-TiO₂ showed an amorphous layer, indicating the successful introduction of OV_s. HRTEM image of Pd_{0.5}-def-TiO₂ (Figure 1c) showed a 3 nm amorphous layer, which was consistent with the existence of OV_s as proven by EPR spectra. The lattice fringe of $d = 0.36\ \text{nm}$ was indexed to the (101) facet of anatase TiO₂. Figure 1d displayed the fast Fourier transform (FFT) image of Pd_{0.5}-def-TiO₂, in which the diffraction rings could be indexed as (101), (200) facet of TiO₂, and (111) facet of Pd. Energy dispersive spectroscopy (EDS)-mapping images showed the elemental distribution of O, Pd, and Ti (Figure 1e), which further proved the successful introduction of Pd nanoparticles. Moreover, specific surface area (S_{BET}) was measured by the nitrogen adsorption-desorption isotherms (Figure S2, Supporting Information).

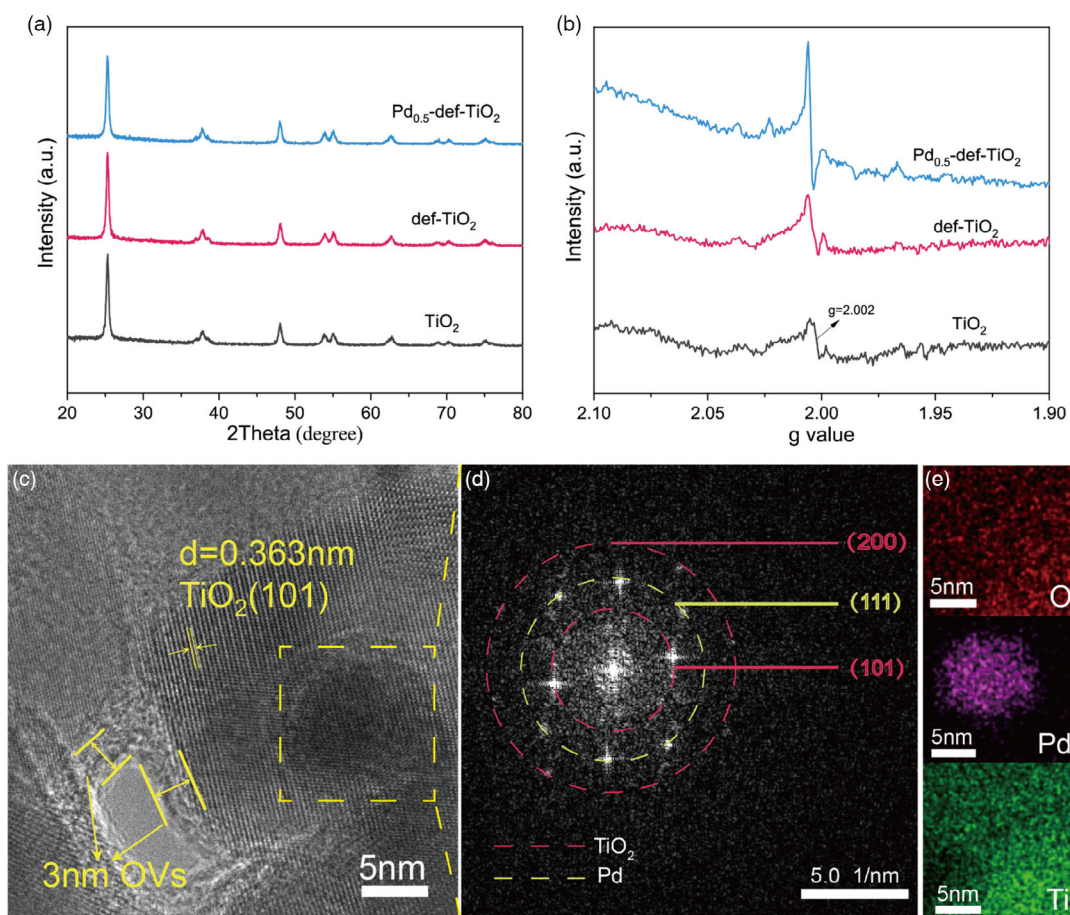


Figure 1. a) X-ray diffraction (XRD) patterns and b) electron paramagnetic resonance (EPR) spectra of TiO₂, def-TiO₂, and Pd_{0.5}-def-TiO₂ samples. c) High-resolution transmission electron microscope (HRTEM) image, d) fast Fourier transform (FFT) image, and e) EDS-mapping images of Pd_{0.5}-def-TiO₂. Red, purple, and green color represent O, Pd, and Ti elements, respectively.

No obvious difference in S_{BET} was detected, implying that surface area would not be the main factor for the improvement of catalytic CH_4 conversion investigated later.

2.2. Photocatalytic CH_4 Conversion

Photocatalytic activity was evaluated by CH_4 conversion conducted in a stainless-steel autoclave reactor with the top irradiation. The detailed oxygenate production was summarized in

Table S2, Supporting Information. The targeted C1 products included CH_3OH , CH_3OOH , and HCHO , while CO_2 was regarded as the overoxidation product. The effect of noble metal species was studied by loading Pt, Au, Ag, and Pd (0.5 wt%) on def-TiO₂ (Figure 2a). Under the same reaction condition, Pt_{0.5}-def-TiO₂, Au_{0.5}-def-TiO₂, and Ag_{0.5}-def-TiO₂ exhibited a similar yield of C1 products at 10 664, 11 705, and 14 885 $\mu\text{mol g}^{-1} \text{h}^{-1}$, respectively. While a much higher performance was observed over Pd_{0.5}-def-TiO₂ (54 693 $\mu\text{mol g}^{-1} \text{h}^{-1}$).

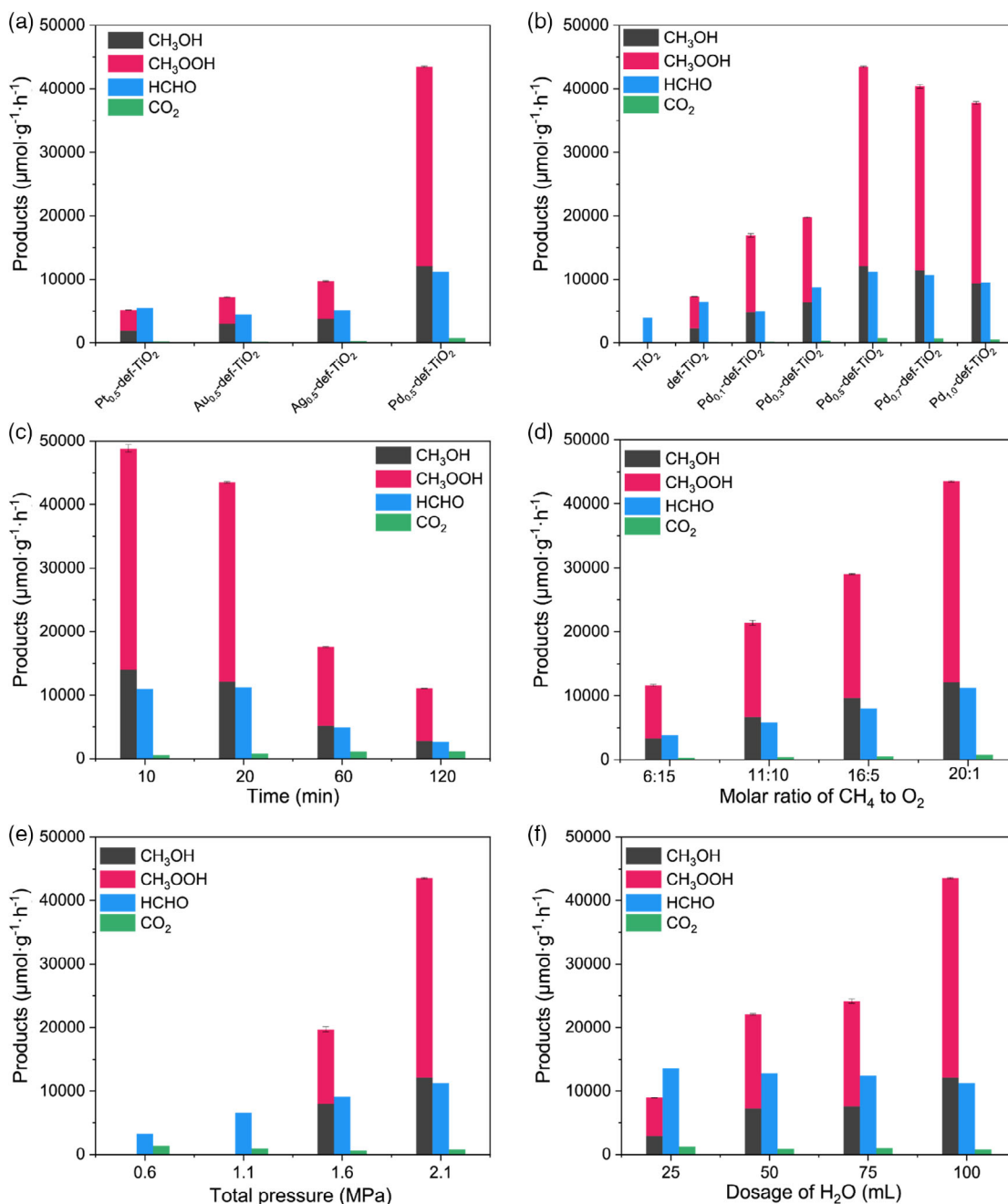


Figure 2. Photocatalytic direct methane conversion over a) different cocatalyst-def-TiO₂ for photocatalytic activity. b) Pd_x-def-TiO₂ for Pd loading content optimization. Investigations on: c) the reaction time, d) the molar ratio of CH_4 to O_2 , e) the total pressure, and f) dosage of H_2O over Pd_{0.5}-def-TiO₂. Reaction conditions: 10 mg catalyst, 100 mL H_2O , 2 MPa CH_4 and 0.1 MPa O_2 for 20 min irradiation with 365 nm light emitting diode (LED) light and maintained at 25 °C.

For the other noble-metal modification including Au, Pt, and Ag, no significant improvements were observed, which is because they were reported as electron acceptors and could not efficiently trap holes for CH₄ oxidation.^[19] Such results indicated that Pd was a more suitable cocatalyst compared with other noble metals to drive CH₄ conversion.

The effect of OVs and the loading amount of Pd on CH₄ conversion were then studied. As observed from Figure 2b, in the absence of OVs, pristine TiO₂ presented a low C1 yield of 3994 μmol g⁻¹ h⁻¹. The relatively low activity was attributed to the severe charge recombination of pristine TiO₂. After modifying with OVs, the yield of C1 products improved to 13 765 μmol g⁻¹ h⁻¹ for def-TiO₂, 3.4 times higher than that of pristine TiO₂, indicating the critical role of OVs in promoting CH₄ conversion. Further modification with Pd cocatalyst resulted in a dramatic enhancement of CH₄ conversion. The C1 yield increased from 21 951 to 54 693 μmol g⁻¹ h⁻¹ as the Pd loading varied from 0.1 to 0.5 wt%. The highest yield of C1 products reached 54 693 μmol g⁻¹ h⁻¹ over the optimal photocatalyst Pd_{0.5}-def-TiO₂, almost 14 and 4 times that of pristine TiO₂ and def-TiO₂. Further increasing Pd content led to the declined yield of C1 products, which might be caused by the enlarged particle size of Pd cocatalysts.^[20] Thus, OVs and the appropriate amount of Pd modification played a vital role in promoting the CH₄ conversion synergistically.^[11b] Reaction conditions including reaction time, the molar ratio of CH₄ to O₂, total pressure, and dosage of H₂O were then investigated on Pd_{0.5}-def-TiO₂. As prolonging reaction time, oxygenates produced and gradually occupied the adsorption sites of CH₄. Therefore, further prolonging the reaction time contributed little to the formation of oxygenates while the improved concentration of oxygenates on the surface easily led to the overoxidation of CO₂, and exhibited the improved production rate of CO₂ from 525 to 1172 μmol g⁻¹ h⁻¹ (Figure 2c). Therefore, the short reaction time was beneficial to obtain higher C1 products. The molar ratio of CH₄ to O₂ was optimized on Pd_{0.5}-def-TiO₂ at a total pressure of 2.1 MPa (Figure 2d). At CH₄/O₂ = 6/15, a relatively low yield of C1 products reaches only 15 483 μmol g⁻¹ h⁻¹. A higher ratio at CH₄/O₂ = 11/10 led to the increased yield to 27 247 μmol g⁻¹ h⁻¹. The yield of C1 products increased to the highest (54 693 μmol g⁻¹ h⁻¹) at CH₄/O₂ = 20/1. Besides, the yield of CO₂ increased from 311 to 768 μmol g⁻¹ h⁻¹ with the gradually increased molar ratio of CH₄ to O₂. Compared with CH₄, the solubility of O₂ in H₂O is higher,^[21] and when the partial pressure of CH₄ increased, the dissolved CH₄ in water increased as well. Therefore, with the increase of dissolved CH₄ in H₂O, the yield of oxygenates generated also increased. Maintaining a constant molar ratio of CH₄ to O₂ (20:1) and lowering the amount of CH₄ and O₂ by lowering the total pressure, the yield of C1 products decreased from 54 693 μmol g⁻¹ h⁻¹ at 2.1 MPa to 3290 μmol g⁻¹ h⁻¹ at 0.6 MPa (Figure 2e). It is clear that the solubility of CH₄ and O₂ plays a crucial role in CH₄ conversion. The dosage of H₂O was then investigated and exhibited in Figure 2f. Along with the increase in H₂O dosage, the yield of C1 products increased from 22 466 to 54 693 μmol g⁻¹ h⁻¹, which is probably attributed to the enhanced mass transfer by water.^[22] The wavelength-dependent AQY of C1 oxygenate products was then measured as 1.05% at 365 nm for Pd_{0.5}-def-TiO₂ (Table S3, Supporting Information).

2.3. Mechanism Investigation

UV-vis diffuse reflectance spectra (UV-DRS) spectra were conducted to determine the light absorbance of the photocatalysts. Compared to TiO₂, def-TiO₂ exhibited a slight improvement in absorption between 395 nm and 540 nm due to oxygen vacancies (Figure 3a). In addition, TiO₂, def-TiO₂, and Pd_{0.5}-def-TiO₂ showed a similar adsorption edge at 380-390 nm, indicating the identical structure of the as-prepared TiO₂-based photocatalysts.

To study the charge transfer of the as-prepared photocatalysts, in situ XPS under light were conducted. Pd_{3d} XPS spectrum of Pd_{0.5}-def-TiO₂ displayed two main peaks located at 340.02 and 334.78 eV, and two minor peaks at 340.87 and 335.82 eV (Figure 3b). The former and the latter were assigned to Pd⁰ and Pd²⁺ species, respectively.^[18a] The content of Pd²⁺ species increased from 18.8% in the dark to 31.5% under irradiation, meanwhile, the content of Pd⁰ species decreased from 81.2% to 68.5%, indicating the role of Pd cocatalyst as the hole acceptor.

The band structure of photocatalysts was measured to figure out whether the catalysts can generate reactive oxygen species (ROS). The bandgap energy (E_B) was calculated to be 3.10 eV of TiO₂, 3.04 eV of def-TiO₂, and 3.00 eV of Pd_{0.5}-def-TiO₂ by the Tauc plots (Figure S3, Supporting Information). As shown in Figure S4, Supporting Information, Mott-Schottky plots were used to measure the flat band potential, which is located below the conduction band (CB) by 0.1 V for n-type semiconductor.^[23] The positive slopes of the three samples indicated that three samples were n-type semiconductors. The correlative CB position worked out at -0.97 V of TiO₂, -0.88 V of def-TiO₂ and -1.05 V of Pd_{0.5}-def-TiO₂ vs Ag/AgCl (pH = 7). Accordingly, the energy level of the valence band (E_V) was attained by $E_V = E_B + E_C$ (E_V , E_B , and E_C are the energy level of the valence band, bandgap, and CB, respectively). Therefore, the corresponding valence band worked out at 2.74 V of TiO₂, 2.77 V of def-TiO₂, and 2.56 V of Pd_{0.5}-def-TiO₂ vs RHE (pH = 0). The band positions with respect to RHE at pH = 0 are shown in Figure S5, Supporting Information. It suggested the band potentials of the catalysts are theoretically sufficient for the generation of ROS.

In situ solid-state EPR spectra were conducted to further elucidate the photogenerated charge dynamics of def-TiO₂ under light (Figure 3c). Under dark condition, the signal at $g = 2.004$ was observed, which was attributed to the OVs.^[24] Under light illumination for 30 s, the signal intensity of OVs enhanced significantly, indicating that after excitation by light, OVs played a vital role in capturing the migrated photo-generated electrons.^[25] However, after illumination for 120 and 240 s, the signal intensity of OVs decreased, which might be the recombination of photogenerated electrons and holes.^[26]

Steady-state PL spectra were conducted to study charge separation behavior (Figure 3d). Pristine TiO₂ exhibited a strong PL emission peak at 475 nm, which was corresponding with the severe charge recombination.^[23] After introducing OVs, the PL emission peak was relatively quenched, indicating that OVs could promote charge separation.^[11c] The weakest PL peak intensity of Pd_{0.5}-def-TiO₂ showed the highest carrier separation efficiency, which was ascribed to the synergistic effect of the OVs and Pd nanoparticles loading. Photocurrent density further

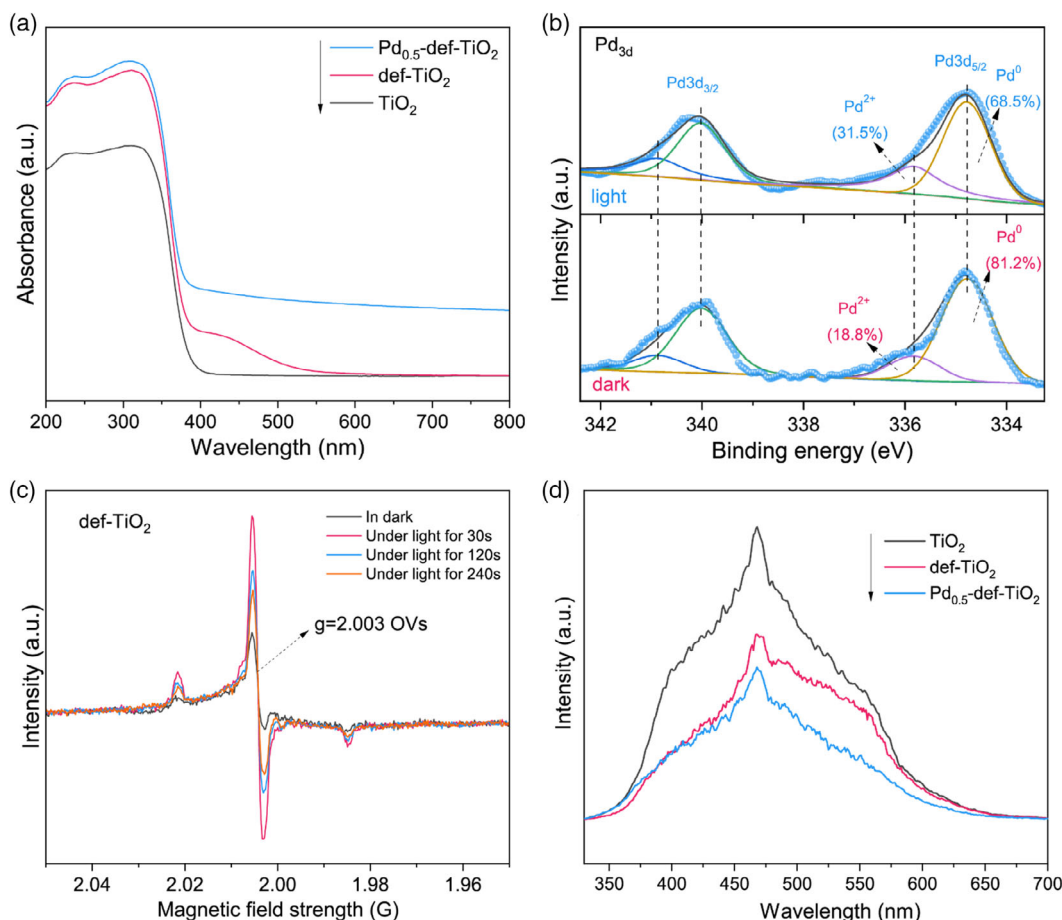


Figure 3. a) UV-vis diffuse reflectance spectra (UV-DRSO) of different photocatalysts. b) Pd 3d X-ray photoelectron spectroscopy (XPS) spectra of Pd_{0.5}-def-TiO₂ under light and in dark. c) EPR spectra of def-TiO₂ under the dark and light condition. d) Photoluminescence (PL) spectra of TiO₂, def-TiO₂, and Pd_{0.5}-def-TiO₂ samples.

confirmed the charge separation efficiency of the photocatalyst (Figure S6, Supporting Information). A low photocurrent density of $113 \mu\text{A cm}^{-2}$ was observed over pristine TiO₂. After OVs decoration, the photocurrent density for def-TiO₂ showed 1.4 times improvement compared with pristine TiO₂. The highest photocurrent intensity was found to be $227 \mu\text{A cm}^{-2}$ for Pd_{0.5}-def-TiO₂, nearly 2.0 times that of pristine TiO₂, indicating the most efficient charge separation efficiency, consistent with the PL analysis. Electrochemical impedance spectroscopy (EIS) showed the smallest radius of the Pd_{0.5}-def-TiO₂ compared with others, representing the lowest polarization resistance, which was more favorable for interfacial charge transfer (Figure S7, Supporting Information).

In situ EPR spectra were used to study the ROS under light over Pd_{0.5}-def-TiO₂ with DMPO as the radical trapping agent. **Figure 4a** exhibited DMPO-OH and DMPO-OOH signals in the presence of Pd_{0.5}-def-TiO₂ under light irradiation, which indicated that ·OH and ·OOH were the ROS during the CH₄ conversion.^[27] ROS generation was further evaluated by using COU and NBT as the ·OH and ·OOH radicals probes, respectively. **Figure 4b** exhibited the fitted kinetic curves of NBT photodegradation, which were used to evaluate the production rate of ·OOH

radicals.^[28] Pristine TiO₂ showed a low kinetic constant at 0.036 min^{-1} , and the constant of def-TiO₂ was improved to 0.10 min^{-1} . The highest constant was 0.18 min^{-1} for Pd_{0.5}-def-TiO₂. Such results demonstrated that Pd_{0.5}-def-TiO₂ exhibited the strongest ability for ·OOH radicals generation. As shown in **Figure 4c**, TiO₂ and def-TiO₂ showed the similar intensity of 7HC after 10 min irradiation, and the relatively low intensity indicated the moderate ability of TiO₂ and def-TiO₂ to generate ·OH radicals. The strongest PL intensity of 7HC was observed over Pd_{0.5}-def-TiO₂, indicating its strongest ability to form the ·OH radicals after 10 min irradiation.

Isotopic labeling experiments over Pd_{0.5}-def-TiO₂ were applied to investigate the oxygen sources for oxygenating production. In the presence of H₂¹⁸O and ¹⁶O₂ (**Figure 4d**), both CH₃¹⁶OH ($m/z = 31, 32$) and CH₃¹⁸OH ($m/z = 33, 34$) were detected suggesting that CH₃OH was formed with both O₂ and H₂O as the oxygen sources. Meanwhile, CH₃¹⁶OH was found as the predominant products, thus demonstrating that O₂ was the main oxygen source for CH₃OH production. Further evidence came from the usage of H₂¹⁶O and ¹⁸O₂ system for CH₄ conversion, where CH₃¹⁸OH was the majority one. It was further confirmed that O₂ was the main oxygen source.

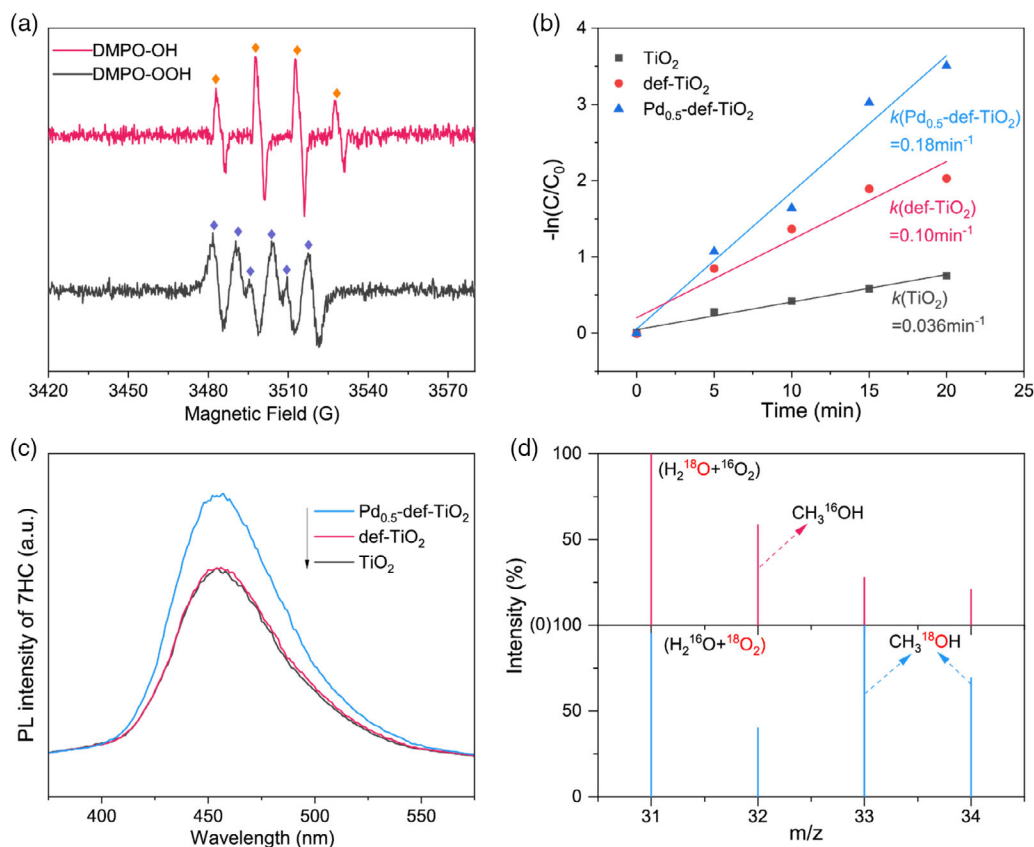
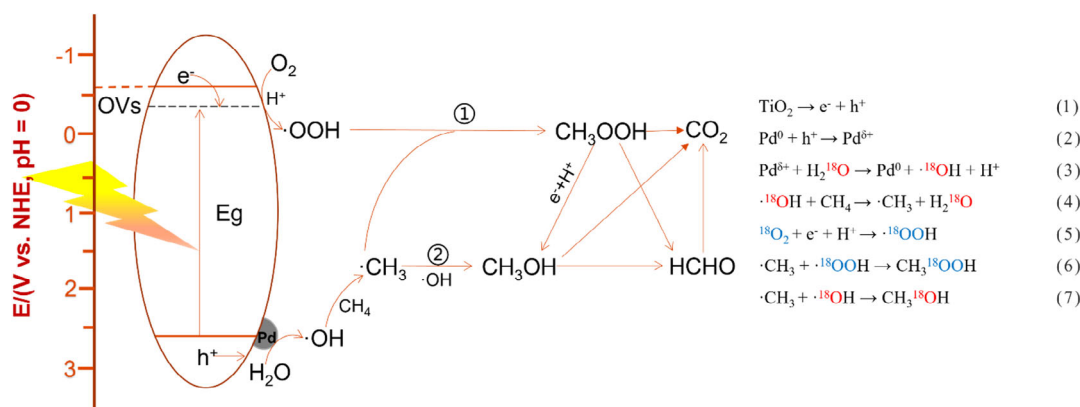


Figure 4. a) In situ EPR spectra of DMPO-OOH and DMPO-OH for monitoring the $\cdot\text{OOH}$ and $\cdot\text{OH}$ radicals. b) The kinetic constant of photodegradation of NBT by $\cdot\text{OOH}$ radicals over TiO_2 , def-TiO_2 , and $\text{Pd}_{0.5}\text{-def-TiO}_2$. c) PL spectra of the 7HC for $\cdot\text{OH}$ radicals measurement over TiO_2 , def-TiO_2 , and $\text{Pd}_{0.5}\text{-def-TiO}_2$ with 10 min irradiation. d) GC-MS spectra of CH_3OH generated over $\text{Pd}_{0.5}\text{-def-TiO}_2$ with $\text{H}_2^{18}\text{O} + ^{16}\text{O}_2$ or $\text{H}_2^{16}\text{O} + ^{18}\text{O}_2$ for CH_4 oxidation.

Based on the aforementioned analysis, the mechanism of photocatalytic CH_4 conversion over the $\text{Pd}_{0.5}\text{-def-TiO}_2$ was proposed in Scheme 1. Electrons were excited to the CB and holes settled on the valence band of $\text{Pd}_{0.5}\text{-def-TiO}_2$ under light irradiation (Equation 1). Then, the holes transferred to the Pd nanoparticle which was confirmed by the in situ XPS spectra and in situ solid-state EPR spectra, activating H_2O to form $\cdot\text{OH}$ radicals (Equation 2 and 3). The existence of $\cdot\text{OH}$ radicals was proved

by the in situ EPR spectra and COU probe detected by PL spectra. In parallel, electrons transferred to the oxygen vacancies and then reduced the adsorbed O_2 to produce $\cdot\text{OOH}$ (Equation 5).^[29] The as-formed $\cdot\text{OH}$ radicals next activated CH_4 into $\cdot\text{CH}_3$ radicals (Equation 4). As the oxygen source for CH_3OH came from both H_2O and O_2 , it was accordingly concluded that $\cdot\text{CH}_3$ radicals reacted with both $\cdot\text{OH}$ radicals and $\cdot\text{OOH}$ radicals (Equation 6 and 7), which were generated from H_2O oxidation and O_2



Scheme 1. Proposed reaction mechanism of photocatalytic CH_4 conversion over $\text{Pd}_{0.5}\text{-def-TiO}_2$.

reduction, respectively. The generation of HCHO^[30] was derived from further oxidation of the as-produced CH₃OOH and CH₃OH.^[7] The overoxidation of C1 oxygenates to CO₂ might be caused by ·OH radicals.

3. Conclusion

In summary, efficient and selective oxidation of CH₄ to form oxygenates over Pd_{0.5}-def-TiO₂ has been achieved under very mild reaction conditions with O₂ and H₂O as the oxidants at room temperature. The C1 products including CH₃OH, CH₃OOH, and HCHO reach a high yield of 54 693 μmol g⁻¹ h⁻¹ with ≈98.6% selectivity. Pd and OVs have been proved to act as the hole and electron acceptors, as confirmed by in situ XPS and EPR under light irradiation, respectively. Consequently, the enhanced charge separation efficiency is achieved over the optimized Pd_{0.5}-def-TiO₂. In addition, both O₂ and H₂O provide the oxygen sources for CH₃OH formation through H₂O oxidation and O₂ reduction, with O₂ as the predominant one. This work thus provides effective guidance for the synergistic effect of metal cocatalysts and OVs on direct CH₄ conversion under mild conditions.

4. Experimental Section

Chemicals: Commercial TiO₂ (anatase phase, 60 nm), potassium hexachloropalladate (IV) (K₂PdCl₆), chloroauric acid (HAuCl₄), chloroplatinic acid (H₂PtCl₆), silver nitrate (AgNO₃), methanol (CH₃OH), barium sulfate (Ba₂SO₄), sodium sulfate (Na₂SO₄), nitrotetrazolium blue chloride (NBT), 5, 5-dimethyl-1-pyrroline-N-oxide (DMPO), and Nafion solution (5 wt%) were purchased from Adamas-Beta. All chemicals were utilized as received without further purification.

Synthesis of OVs-Modified TiO₂: OVs-modified TiO₂ photocatalyst was prepared through the two-step thermal calcination of the mixture of urea and anatase.^[31] Typically, a certain amount of urea and anatase TiO₂ were uniformly grinded in a mortar, and then underwent calcination under a cover at 550 °C for 4 h in ultrapure argon (99.999 vol%) with a heating rate of 2 °C min⁻¹. Afterward, the obtained yellow powder was further calcinated in air at 550 °C for 2 h with a ramp rate of 5 °C min⁻¹. The as-prepared faint yellow product was named as def-TiO₂.

Synthesis of Pd and OVs Co-Modified TiO₂ Photocatalyst: Pd and OVs co-modified TiO₂ photocatalysts were synthesized by the photodeposition method with def-TiO₂ as the substrate.^[32] In a typical experiment, 250 mg def-TiO₂ was suspended in a 30 mL methanol aqueous solution (10 vol%). After being stirred for 5 min, a certain amount of K₂PdCl₆ solution was dropped into the suspension while stirring. After purging with argon, the suspension was sealed and irradiated for 3 h in a multichannel reactor. Photocatalyst was then collected after being centrifuged, washed, and dried at 60 °C. The as-prepared photocatalysts were denoted as Pd_x-def-TiO₂. *x* wt% (*x* = 0.1, 0.3, 0.5, 0.7, 1.0) represented the mass percent of Pd to def-TiO₂. Au, Pt, and Ag were also deposited on def-TiO₂ by the same procedures, except 125 μL HAuCl₄ solution (1 wt%), H₂PtCl₆ solution (1 wt%) or AgNO₃ solution (1 wt%) was dropped into the suspension of def-TiO₂ instead of K₂PdCl₆. Actual metal contents (Table S1, Supporting Information) were measured by an inductively coupled plasma atomic emission spectrometer (ICP-AES).

Characterizations: XRD patterns were measured by a D8 ADVANCE diffractometer (Bruker Co., Ltd) using Cu Kα radiation. HRTEM and EDS-mapping images were recorded on the Talos F200X instrument (FEI Co., Ltd). Nitrogen physical adsorption-desorption isotherms were measured on TRII Star 3020 gas adsorption analyzer at -196 °C. Before measurement, the samples were degassed at 150 °C overnight and back-filled with nitrogen. X-ray photoelectron spectroscopy (XPS) spectra were

measured on the PHI5000Versa ProbelII instrument (ULVAC-PHI Co., Ltd) with an Al Kα excitation source. Taking BaSO₄ as a reference, UV-DRS were taken on a UV-3600 plus spectrometer (Shimadzu Co., Ltd). In situ XPS results under light irradiation were obtained on the Thermo Scientific ESCALAB 250Xi with an Al Kα radiation source. Steady-state photoluminescence (PL) spectra were obtained on the F-4500 spectrofluorometer with the excitation wavelength at 330 nm. Time-resolved PL spectra were acquired on the FLSP920 spectrofluorometer. Solid-state EPR curves were measured on the ELEXSYS II instrument (Bruker Co., Ltd). Photoelectrochemical properties were measured on the CHI660E electrochemical workstation in 0.1 M Na₂SO₄ solution. Ag/AgCl electrode and platinum sheet electrode were used as the reference electrode and counter electrode, respectively. The working electrodes were made from 0.2 g photocatalysts, 0.1 mL Nafion solution, and ethanol. The specific procedure was to mix the powder and the solution evenly and then cover the ITO electrodes by scraping. 300 W Xe lamp (PLS-SXE300D, Beijing Perfectlight Technology Co., Ltd.) was used as the light source during measurement.

Photocatalytic CH₄ Conversion: Photocatalytic CH₄ conversion reaction was conducted in a 200 mL stainless-steel autoclave reactor equipped with a top quartz window. LED lamp (365 nm, PLS-LED100B, Beijing Perfectlight Technology Co., Ltd.) was used as the light source. In a typical test, 10 mg catalyst was dispersed uniformly in 100 mL water through ultrasonication, then the reactor was sealed and purged with ultrapure O₂ (99.999 vol%) for 20 min. Afterward, 2.0 MPa CH₄ (99.999 vol%) and 0.1 MPa O₂ (99.999 vol%) were injected into the reactor. The reaction was conducted for 20 min at 25 °C with a circulating cooling device. Gaseous products, as well as CH₃OH in the reactant, were detected by gas chromatograph (GC-2014, Shimadzu Co., Ltd.) equipped with a thermal conductivity detector (TCD) and flame ionization detector (FID). CH₃OOH was measured by the ¹H nuclear magnetic resonance (¹H NMR) spectroscopy (AVANCE III JEOL Ltd). As CH₃OOH and CH₃OH have the same amount of methyl, the molar ratio of CH₃OOH/CH₃OH should be regarded as the area ratio in ¹H NMR results. HCHO was quantified by the colorimetric method.^[33] Typically, 100 mL color reagent was first prepared by the mixture of 15.0 g ammonium, 0.3 mL acetic acid, and 0.2 mL diacetyl methane. Then, 1.0 mL liquid product was mixed with 4.0 mL distilled water and 1 mL of the above color reagent, which was then maintained at 35 °C for 1 h. The absorbance of the solution was then measured by UV-vis absorption spectroscopy (UV-3600 plus, Shimadzu Co., Ltd) and used for the quantification of HCHO.

Isotope Labeling Experiment: For the detection of oxygen-source in the products using isotopic labeled H₂¹⁸O: 20 mg Pd_{0.5}-def-TiO₂ photocatalyst was dispersed in 2 mL H₂¹⁸O (99%). The reactor was then degassed for 30 min to completely remove air, and then was refilled with 2.0 MPa CH₄ (99.999 vol%) and 0.1 MPa ¹⁶O₂ (99.999 vol%). The reaction was carried out at 25 °C for 6 h. The products were measured by gas chromatography-mass spectrometer (GC-MS) (QP2020, Shimadzu Co., Ltd) equipped with a Cap WAX column.

For the detection of oxygen-source in the products using isotopically labeled ¹⁸O₂: 20 mg Pd_{0.5}-def-TiO₂ photocatalyst was dispersed in 2 mL H₂¹⁶O. The reactor was then degassed for 30 min to completely remove air, and then was refilled with 2.0 MPa CH₄ (99.999 vol%) and 0.1 MPa ¹⁸O₂ (98%). The reaction was carried out at 25 °C for 6 h. The products were measured by GC-MS (QP2020, Shimadzu Co., Ltd) which was equipped with the Cap WAX column.

Measurement of Apparent Quantum Yield: The apparent quantum yield (AQY) was measured over TiO₂, def-TiO₂, and Pd_{0.5}-def-TiO₂ under 365 nm irradiation with the Xe lamp equipped with a band-pass filter as the light source. Light intensity was measured as 74.0 mW cm⁻² by the light intensity meter (PL-MW2000, Beijing Perfectlight Technology Co., Ltd). As the formations of CH₃OOH, CH₃OH, and HCHO need 1, 3, and 5 photogenerated charges, respectively,^[7] AQY was calculated by the following equation.

$$AQY = \frac{N(\text{CH}_3\text{OOH}) + N(\text{CH}_3\text{OH}) \times 3 + N(\text{HCHO}) \times 5}{N(\text{photons})} \times 100\% \quad (1)$$

$N(\text{CH}_3\text{OOH})$, $N(\text{CH}_3\text{OH})$, and $N(\text{HCHO})$ represented the number of CH_3OOH , CH_3OH , and HCHO . $N(\text{photons})$ represented the number of incident photons.

Monitoring of Hydroxyl Radicals (OH) and Hydroperoxyl Radicals (OOH): In situ EPR was applied to monitor the generation of $\cdot\text{OH}$ and $\cdot\text{OOH}$ radicals under light irradiation.^[33b,34] For the detection of $\cdot\text{OH}$ radicals, 10 mg catalyst was suspended in 5 mL water, with DMPO as the trapping agent. For detecting the $\cdot\text{OOH}$ radicals, 10 mg catalyst was suspended in 5 mL methanol, with DMPO as the trapping agent as well.

NBT photodegradation method was applied to measure the $\cdot\text{OOH}$ radicals.^[28a,35] Briefly, 25 mg photocatalyst was first dispersed in the 100 mL NBT aqueous solution (0.02 mM) in dark for 20 min to achieve adsorption–desorption equilibrium. Then the suspension was irradiated with a 365 nm LED lamp and sampled every five minutes, which was measured on the UV-3600 Plus spectrometer after being filtered.

The PL technique was applied to measure the $\cdot\text{OH}$ radicals according to the reaction between $\cdot\text{OH}$ and coumarin (COU) to generate 7-hydroxycoumarin (7HC), which could be detected by PL spectra at 450 nm^[36] Briefly, 25 mg catalyst was dispersed in the 100 mL COU aqueous solution (0.5 mM). Before illumination, the mixture was stirred in dark for 30 min to achieve the adsorption–desorption equilibrium. During light illumination, the suspension was sampled, and filtered at 5 min intervals. Then, the solution was detected by the F4500 spectrofluorometer.

Supporting Information

Supporting Information is available from the Wiley Online Library or from the author.

Acknowledgements

Z.G. and L.L. are grateful for the China Postdoctoral Science Foundation (Grant No. 2019M663802) and the Shaanxi Key Research Grant (China, 2020GY-244). C.W. and J.T. are thankful for financial support from the UK EPSRC (EP/S018204/2), Leverhulme Trust (RPG-2017-122), the Royal Society Newton Advanced Fellowship grant (NAF\R1\191163), and the Royal Society Leverhulme Trust Senior Research Fellowship (SRF\R1\21000153).

Conflict of Interest

The authors declare no conflict of interest.

Data Availability Statement

The data that support the findings of this study are available from the corresponding author upon reasonable request.

Keywords

charge separation, direct methane conversion, high selectivity, oxygen vacancies, Pd cocatalysts

Received: April 15, 2022
Revised: August 16, 2022
Published online:

- [1] a) X. Li, C. Wang, J. Tang, *Nat. Rev. Mater.* **2022**, *1*, 617; b) P. Schwach, X. Pan, X. Bao, *Chem. Rev.* **2017**, *117*, 8497; c) M. Ravi, M. Ranocchiaro, V. Bokhoven, *Angew. Chem. Int. Ed.* **2017**, *56*, 16464.

- [2] H. Song, X. Meng, Z. Wang, H. Liu, J. Ye, *Joule* **2019**, *3*, 1606.
[3] a) S. Das, J. Ashok, Z. Bian, N. Dewangan, M. H. Wai, Y. Du, A. Borgna, K. Hidajat, S. Kawi, *Appl. Catal., B* **2018**, *230*, 220; b) J. M. Lavoie, *Front. Chem.* **2014**, *2*, 81.
[4] a) H. Jahangiri, J. Bennett, P. Mahjoubi, K. Wilson, S. Gu, *Catal. Sci. Technol.* **2014**, *4*, 2210; b) J. Li, Y. He, L. Tan, P. Zhang, X. Peng, A. Oruganti, G. Yang, H. Abe, Y. Wang, N. Tsubaki, *Nat. Catal.* **2018**, *1*, 787.
[5] H. M. Torres Galvis, K. P. de Jong, *ACS Catal.* **2013**, *3*, 2130.
[6] a) L. Luo, Z. Gong, Y. Xu, J. Ma, H. Liu, J. Xing, J. Tang, *J. Am. Chem. Soc.* **2022**, *144*, 740; b) L. Luo, L. Fu, H. Liu, Y. Xu, J. Xing, C. R. Chang, D. Y. Yang, J. Tang, *Nat. Commun.* **2022**, *13*, 2930.
[7] H. Song, X. Meng, S. Wang, W. Zhou, X. Wang, T. Kako, J. Ye, *J. Am. Chem. Soc.* **2019**, *141*, 20507.
[8] L. Luo, J. Luo, H. Li, F. Ren, Y. Zhang, A. Liu, W. X. Li, J. Zeng, *Nat. Commun.* **2021**, *12*, 1218.
[9] a) J. Wan, W. Chen, C. Jia, L. Zheng, J. Dong, X. Zheng, Y. Wang, W. Yan, C. Chen, Q. Peng, D. Wang, Y. Li, *Adv. Mater.* **2018**, *30*, 1705369; b) W. Jiang, J. Low, K. Mao, D. Duan, S. Chen, W. Liu, C. W. Pao, J. Ma, S. Sang, C. Shu, X. Zhan, Z. Qi, H. Zhang, Z. Liu, X. Wu, R. Long, L. Song, Y. Xiong, *J. Am. Chem. Soc.* **2021**, *143*, 269; c) X. Li, J. Xie, H. Rao, C. Wang, J. Tang, *Angew. Chem. Int. Ed.* **2020**, *59*, 19702.
[10] a) D. Zhao, C. L. Dong, B. Wang, C. Chen, Y. C. Huang, Z. Diao, S. Li, L. Guo, S. Shen, *Adv. Mater.* **2019**, *31*, e1903545; b) R. Shi, Y. Zhao, G. I. N. Waterhouse, S. Zhang, T. Zhang, *ACS Catal.* **2019**, *9*, 9739; c) Z. Yang, Y. Shi, H. Li, C. Mao, X. Wang, X. Liu, X. Liu, L. Zhang, *Environ. Sci. Technol.* **2022**, *56*, 3587–3595.
[11] a) K. H. Kim, C.-W. Choi, S. Choung, Y. Cho, S. Kim, C. Oh, K.-S. Lee, C.-L. Lee, K. Zhang, J. W. Han, S.-Y. Choi, J. H. Park, *Adv. Energy Mater.* **2022**, *12*, 2103495; b) J.-Y. Qiu, H.-Z. Feng, Z.-H. Chen, S.-H. Ruan, Y.-P. Chen, T.-T. Xu, J.-Y. Su, E.-N. Ha, L.-Y. Wang, *Rare Metals* **2022**, *41*, 2074; c) S. Yao, J. Liu, F. Liu, B. Wang, Y. Ding, L. Li, C. Liu, F. Huang, J. Fang, Z. Lin, M. Wang, *Environ. Sci.: Nano* **2022**, *9*, 1996.
[12] a) M. J. Torralvo, J. Sanz, I. Sobrados, J. Soria, C. Garlisi, G. Palmisano, S. Çetinkaya, S. Yurdakal, V. Augugliaro, *Appl. Catal., B* **2018**, *221*, 140; b) B. Wang, M. Zhang, X. Cui, Z. Wang, M. Rager, Y. Yang, Z. Zou, Z. L. Wang, Z. Lin, *Angew. Chem. Int. Ed.* **2020**, *59*, 1611.
[13] a) L. Liu, H. Zhao, J. M. Andino, Y. Li, *ACS Catal.* **2012**, *2*, 1817; b) Z. Mo, H. Xu, Z. Chen, X. She, Y. Song, J. Lian, X. Zhu, P. Yan, Y. Lei, S. Yuan, H. Li, *Appl. Catal., B* **2019**, *241*, 452.
[14] H. Song, X. Meng, S. Wang, W. Zhou, S. Song, T. Kako, J. Ye, *ACS Catal.* **2020**, *10*, 14318.
[15] R. Yang, S. L. Liu, H. T. Wang, Z. M. Lun, X. Zhou, C. P. Zhao, C. G. Min, H. Zhang, Y. Xu, D. F. Zhang, *Ind. Eng. Chem. Res.* **2021**, *60*, 15817.
[16] G. J. Hutchings, *Top. Catal.* **2016**, *59*, 658.
[17] T. Hou, Q. Li, Y. Zhang, W. Zhu, K. Yu, S. Wang, Q. Xu, S. Liang, L. Wang, *Appl. Catal., B* **2020**, *273*, 119072.
[18] a) C. Wang, Y. Li, C. Zhang, X. Chen, C. Liu, W. Weng, W. Shan, H. He, *Appl. Catal., B* **2021**, *282*, 119540; b) X. Wang, Z. Rui, Y. Zeng, H. Ji, Z. Du, Q. Rao, *Catal. Today* **2017**, *297*, 151.
[19] a) W. Zhu, Z. Wu, G. S. Foo, X. Gao, M. Zhou, B. Liu, G. M. Veith, P. Wu, K. L. Browning, H. N. Lee, H. Li, S. Dai, H. Zhu, *Nat. Commun.* **2017**, *8*, 15291; b) Q.-Q. Yan, D.-X. Wu, S.-Q. Chu, Z.-Q. Chen, Y. Lin, M.-X. Chen, J. Zhang, X.-J. Wu, H.-W. Liang, *Nat. Commun.* **2019**, *10*, 4977.
[20] R. K. Ramachandran, J. Dendooven, M. Filez, V. V. Galvita, H. Poelman, E. Solano, M. M. Minjauw, K. Devloo-Casier, E. Fonda, D. Hermida-Merino, W. Bras, G. B. Marin, C. Detavernier, *ACS Nano* **2016**, *10*, 8770.

- [21] C. Liu, H. Chou, C. Lin, D. Janmanchi, P. Chung, C. Mou, S. S. F. Yu, S. I. Chan, *Microporous Mesoporous Mater.* **2020**, 293, 109793.
- [22] S. Lee, K. Mo, J. Choi, N. H. Hur, Y. Kim, B. Oh, J. Lee, *Korean J. Chem. Eng.* **2015**, 32, 1744.
- [23] H. Tan, Z. Zhao, M. Niu, C. Mao, D. Cao, D. Cheng, P. Feng, Z. Sun, *Nanoscale* **2014**, 6, 10216.
- [24] J. Nie, J. Schneider, F. Sieland, S. Xia, D. W. Bahnemann, *J. Photochem. Photobiol., A* **2018**, 366, 111.
- [25] J. B. Priebe, M. Karnahl, H. Junge, M. Beller, D. Hollmann, A. Brückner, *Angew. Chem., Int. Ed.* **2013**, 52, 11420.
- [26] S. Bai, N. Zhang, C. Gao, Y. Xiong, *Nano Energy* **2018**, 53, 296.
- [27] a) L. Lin, M. Danilczuk, S. Schlick, *J. Power Sources* **2013**, 233, 98; b) S. Pei, S. You, J. Ma, X. Chen, N. Ren, *Environ. Sci. Technol.* **2020**, 54, 13333.
- [28] a) X. Ran, L. Duan, X. Chen, X. Yang, *J. Mater. Sci.* **2018**, 53, 7048; b) Y. Qi, J. Ye, S. Zhang, Q. Tian, N. Xu, P. Tian, G. Ning, *J. Alloys Compd.* **2019**, 782, 780.
- [29] a) W. Zhou, X. Qiu, Y. Jiang, Y. Fan, S. Wei, D. Han, L. Niu, Z. Tang, *J. Mater. Chem. A* **2020**, 8, 13277; b) K. Li, A. D. Handoko, M. Khraisheh, J. Tang, *Nanoscale* **2014**, 6, 9767.
- [30] T. J. Miao, C. Wang, L. Xiong, X. Li, J. Xie, J. Tang, *ACS Catal.* **2021**, 11, 8226.
- [31] W. Jiang, X. Zong, L. An, S. Hua, X. Miao, S. Luan, Y. Wen, F. F. Tao, Z. Sun, *ACS Catal.* **2018**, 8, 2209.
- [32] A. Tanaka, K. Hashimoto, H. Kominami, *J. Am. Chem. Soc.* **2012**, 134, 14526.
- [33] a) J. Chen, S. Stepanovic, A. Draksharapu, M. Gruden, W. R. Browne, *Angew. Chem. Int. Ed.* **2018**, 57, 3207; b) Y. Nosaka, A. Y. Nosaka, *Chem. Rev.* **2017**, 117, 11302.
- [34] H. Hou, X. Zeng, X. Zhang, *Angew. Chem., Int. Ed.* **2020**, 59, 17356.
- [35] A. C. Maier, E. H. Iglebaek, M. Jonsson, *ChemCatChem* **2019**, 11, 5435.
- [36] W. C. Huo, X. A. Dong, J. Y. Li, M. Liu, X. Y. Liu, Y. X. Zhang, F. Dong, *Chem. Eng. J.* **2019**, 361, 129.